Materials Advances

ROYAL SOCIETY OF CHEMISTRY

PAPER

View Article Online
View Journal | View Issue

Cite this: *Mater. Adv.*, 2024, 5, 8864

Eco-friendly repurposing of by-pass waste for optics and radiation protection: addressing hazardous material challenges

Hesham M. H. Zakaly, *[abc] H. Hashim,[d] Shams A. M. Issa,[ef] Moustafa A. Darwish, *[d] Fatma M. Obiedallah,[g] M. S. I. Koubisy[e] and H. A. Saudi[h]

This study delves into the investigation of the optical and gamma radiation shielding properties of glasses formulated with varying concentrations of by-pass (cement dust) combined with Na_2O, Fe_2O_3, Bi_2O_3, and P_2O_5. The specific compositions are represented as ((*x*) by-pass–(20) Na_2O–(10) Fe_2O_3–(20) Bi_2O_3–(50 − *x*) P_2O_5), with "*x*" ranging from 0 to 15 wt%. The structural and optical properties of these glasses were analyzed using X-ray diffraction (XRD), Fourier-transform infrared (FTIR) spectroscopy, and UV-visible-NIR spectroscopy techniques. The XRD results reveal the absence of Bragg peaks and highlight the amorphous nature of the prepared samples. Notably, increasing by-pass concentration enhanced UV-visible-NIR transmittance, particularly from 400 nm to 850 nm. Radiation shielding assessments were conducted across photon energies ranging from 80 to 2614 keV. The results highlighted that the linear and mass attenuation coefficients were inversely proportional to the photon energy. The by-pass15 glass, with the highest by-pass concentration, consistently demonstrated superior shielding attributes compared to its counterparts, with the lowest half-value layer (G_{HVL}) values and the most substantial radiation protection efficiency (RPE). Comparative assessments with other glasses and concrete types further accentuated the potential of the by-pass15 glass as a promising candidate for gamma radiation shielding applications. The results obtained in this research pave the way for potentially utilizing by-pass15 glass in environments where radiation protection is imperative. Incorporating by-pass in glass composites enhances their gamma shielding efficiency and promotes the sustainable use of by-pass, underscoring the dual advantages of this innovative approach.

Received 21st May 2024,
Accepted 30th July 2024

DOI: 10.1039/d4ma00519h

rsc.li/materials-advances

1. Introduction

Environmental preservation is an imperative responsibility for the global community in the current era. The escalating concerns about ecological degradation, mainly driven by improper disposal of industrial wastes and the proliferation of harmful materials, have called for innovative strategies to transform potential pollutants into beneficial products. This eco-conscious shift from waste generation to sustainable utilization is not just about conservation; it is about ushering in a new epoch of sustainable development.[1,2] One such promising avenue is the transformation of harmful industrial by-products into high-value materials with exceptional properties. Glass, an ancient material with diverse applications, presents a unique opportunity. Traditionally valued for its transparency and malleability, recent advancements have expanded its utility to optics and radiation shielding realms. Modern glass formulations doped with specific elements or compounds can exhibit remarkable optical characteristics, making them indispensable in advanced applications ranging from optoelectronics to photonics.[3–6]

Radioactive isotopes and related technologies significantly influence modern human life. Naturally occurring isotopes serve as a source of radiation and have various applications. Their detectable radioactivity makes them ideal tracers. They can also eliminate harmful agents from food due to the energy they emit. Moreover, isotopes have diverse medical roles, such as using radioactive ^{131}I to assess thyroid functionality.[7,8]

[a] *Institute of Physics and Technology, Ural Federal University, Yekaterinburg, 620002, Russia. E-mail: h.m.zakaly@gmail.com*
[b] *Istinye University, Faculty of Engineering and Natural Sciences, Computer Engineering Department, Istanbul, 34396, Turkey*
[c] *Department of Physics and Technical Sciences, Western Caspian University, Baku, Azerbaijan*
[d] *Physics Department, Faculty of Science, Tanta University, Tanta 31527, Egypt. E-mail: mostafa_ph@science.tanta.edu.eg*
[e] *Physics Department, Faculty of Science, Al-Azhar University, Assiut Branch, 71524, Egypt*
[f] *Physics Department, Faculty of Science, University of Tabuk, Tabuk, 71451, Saudi Arabia*
[g] *Physics Department, Faculty of Science, Assiut University, Assiut 71516, Egypt*
[h] *Physics Department, Faculty of Science (Girls Branch), Al-Azhar University, Egypt*

Yet, unintended radiation exposure from these isotopes can harm living organisms and the environment. The potential harm depends on the type and amount of energy they release. For example, high doses can lead to conditions like cataracts, DNA damage, infertility, and several diseases.[9] Thus, those handling radioactive materials are advised to use shielding materials to minimize exposure risks.[10–12] Historically, due to their high atomic numbers and density, materials like lead, concrete, and lead composite have been favored for nuclear safety applications. However, concerns like toxicity have limited the use of lead products.[13] This has prompted the search for alternative materials. In this quest, glass systems emerge as potential candidates. They offer advantages over other materials, such as cost-effectiveness, ease of fabrication, recyclability, and light transparency.[14] Specifically, glasses infused with heavy metal oxides, like Bi_2O_3, are gaining traction. Their high density and unique features make them apt for radiation shielding tasks.[15–18]

In recent years, exploring silicate structural, optical, and radiation shielding properties of studies such as the innovative doping of soda-lime-silica glasses with organic compounds like peanut shell powder have opened new avenues for modifying optical properties while promoting sustainability.[19] Further investigations, as documented,[20,21] have delved into the complex interplay between glass composition and its impact on light transmission and radiation protection efficiency. Recent work highlighted[22] has also contributed to our understanding of the structural characteristics crucial for developing non-toxic, eco-friendly radiation shielding materials. These studies underscore the importance of continuous innovation in glass science, particularly in leveraging various dopants and waste materials, to achieve enhanced performance in optical applications and radiation shielding.[23–26]

This research examines the usefulness of prepared glasses in shielding applications at different photon energies. The primary focus of the current study is to experimentally investigate the radiation attenuation characteristics of by-pass (cement dust) glasses, which comprise SiO_2, Al_2O_3, Fe_2O_3, TiO_2, CaO, MgO, Na_2O, and K_2O. For gamma, the effect of systematically replacing by-pass with P_2O_5 on the attenuation characteristics was dissected in great depth. This study also provides a wide-scope comparison of the shielding performance of the current recommended system with that of the typically employed systems. The selection of by-pass waste as a primary material in the present study was driven by multiple factors. First and foremost, by-pass waste, a by-product of the cement industry, poses significant environmental challenges due to its large volume generation and disposal issues.[22,27,28] Its composition, rich in silica and alumina, alongside other oxides such as calcium oxide and iron oxide, makes it a potential candidate for glass synthesis, leveraging its waste-to-wealth conversion potential.[29,30] Furthermore, incorporating by-pass waste into glass composites aligns with global efforts towards sustainable development by reducing landfill use and promoting the recycling of industrial by-products.[31] Additionally, previous studies have indicated that certain waste materials can enhance the optical and radiation-shielding properties of glasses. Therefore, by-pass waste was selected to investigate its efficacy in improving these properties while addressing environmental conservation and waste management challenges. Beyond optics, there is an emergent demand for materials that can shield against harmful radiation, especially in medical, industrial, and nuclear domains. With the growing reliance on nuclear energy and medical radiation, ensuring safety has become paramount. Herein lies the novelty of re-engineering harmful by-products into specialized glass composites that can attenuate harmful radiations. Such advancements address the pressing issue of waste management and provide solutions to critical challenges in radiation protection.

In essence, the convergence of environmental protection with the creation of high-performance materials represents a pioneering approach. It signifies the dawning of an era where harmful residues are no longer discarded but are transformed, through the alchemy of science and innovation, into materials that protect, serve, and inspire. This research underscores the importance and potential of such transformations, highlighting the dual benefits: safeguarding our environment while meeting the demands of cutting-edge technological applications.

2. Materials and methods

2.1. Sample preparation

Cement dust, characterized as by-pass, was sourced from cement factories located in Beni Suef (Egypt). Recognized as industrial waste, this waste (dust) was first analyzed using X-ray fluorescence (XRF) to determine its chemical composition. The predominant elements in the by-pass included 47.67% SiO_2, 4.24% Al_2O_3, 2.14% Fe_2O_3, 0.20% TiO_2, 37.95% CaO, 3% MgO, 2.95% Na_2O, and 1.85% K_2O, cumulatively accounting for 100% of its total oxide content.

By-pass and transparent glasses were synthesized using a specific composition: ((x) by-pass–(20) Na_2O–(10) Fe_2O_3–(20) Bi_2O_3–$(50 - x)$ P_2O_5), where "x" varied as 0 (by-pass0), 3 (by-pass3), 6 (by-pass6), 10 (by-pass10), and 15 (by-pass15) wt%. The glass samples were created through the conventional melt-quenching technique. Five distinct concentrations of the by-pass mixture were initially prepared according to the given composition formula, with "x" ranging from 0 to 15 wt%. The mixtures were continuously stirred at room temperature to achieve homogeneity. Subsequently, the samples were heated to 1450 °C and melted for two hours. The molten samples were poured onto a stainless-steel bar to form the desired shapes. This was followed by a transfer to a secondary furnace set at 300 °C for annealing. The samples were gradually cooled to room temperature, ensuring their structural integrity and amorphous nature.

2.2. Characterizations and measurements

The structural and optical characteristics of the prepared samples were meticulously examined through X-ray diffraction (XRD) using an AXS D8 Advance apparatus (Bruker, Germany), utilizing Cu-K_α radiation at a wavelength of 1.54 Å (λ), within

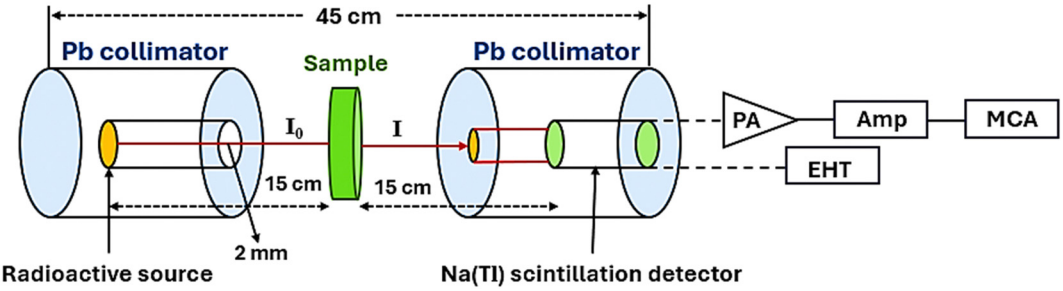

Fig. 1 Experimental radiation measurement setup.

the 2θ range of 10° to 89.6°. In parallel, Fourier-transform infrared (FTIR) spectroscopy was performed using a Bruker Tensor 27 system to map the vibrational spectra of the prepared samples across the spectral range of 1700 cm^{-1} to 450 cm^{-1}. Furthermore, the optical transmission properties were rigorously quantified using a Shimadzu UV-2450 (UV-visible-NIR) spectrophotometer, covering a spectral domain from 200 to 2500 nm. The narrow beam approach, combined with a lead-collimator, was utilized to acquire experimentally established linear attenuation coefficients (G_{LAC}). The values were acquired using a NaI(Tl) scintillation detector with a measurement area of 3 inches by 3 inches coupled to a multichannel analyzer. Throughout the experiment, the following radioactive sources were utilized: ^{133}Ba (5 μCi, 80 keV), ^{137}Cs (5 μCi, 662 keV), ^{60}Co (10 μCi, 1173 and 1333 keV), and ^{232}Th (20 μCi, 238, 911, and 2614 keV). Fig. 1 illustrates the experimental setup, which includes the source, the sample, and the detector in their appropriate locations. Calculations were performed to estimate the photon intensity without and with the absorber for each gamma line using the region underneath the photopeak. These calculations were essential to determine the photon intensity. The process was repeated five times, and 10 minutes was set aside for each iteration of the method. The level of uncertainty was far lower than one percent.

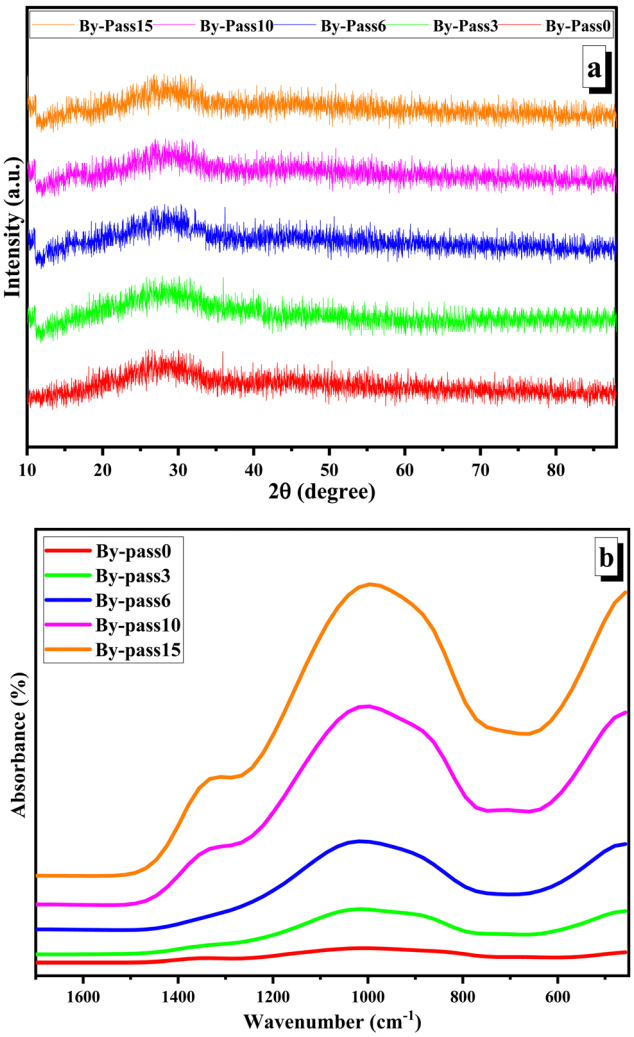

Fig. 2 (a) XRD patterns and (b) FTIR spectra for different by-pass concentrations.

3. Results and discussion

3.1. XRD and FTIR analyses

The XRD patterns of the prepared by-pass glass samples exhibited a remarkable similarity, characterized by the absence of Bragg peaks, as illustrated in Fig. 2(a). This absence of peaks confirms the amorphous nature of the glassy phase of the samples, where the amorphous regions would contribute a broad, low-intensity background. Additionally, no discernible peak corresponding to by-pass was observed, which reveals that the added quantity of by-pass has been fully incorporated into the glass matrix.[32,33]

The FTIR spectra of by-pass cement dust incorporated into phosphate glass matrices reveal significant structural modifications with varying by-pass contents, as shown in Fig. 2(b). The spectra, ranging from 600 cm^{-1} to 1600 cm^{-1}, display distinct absorbance bands associated with Si–O–Si, P–O–P, and P–O vibrational modes. As the by-pass concentration increases from 0% to 15%, notable shifts and intensity changes in these bands occur, which indicate progressive integration of cement dust components into the glass network. These modifications suggest the formation of new structural units or phases, particularly due to incorporating elements such as CaO, MgO, and Al_2O_3.[22] The observed peaks between 800 and 1300 cm^{-1} may be due to P–O–P and Si–O–Si asymmetric stretching.[30] A peak around 1333 cm^{-1} belongs to the asymmetric stretching of

carbonate groups,[34] which only appears in by-pass10 and by-pass15, which is well-matched with a previous study.[31] The systematic spectral variations highlight the effectiveness of the melt-quenching technique in achieving homogeneity and structural integrity in the synthesized glasses. Understanding these changes provides insights into developing advanced glass materials with tailored properties, potentially enhancing their waste management and construction applications.

3.2. Optical properties

3.2.1. UV-visible-NIR spectroscopy analysis. The UV-visible-NIR spectroscopy analysis, conducted on samples with a thickness of 0.43 cm, is illustrated in Fig. 3(a). Analysis of the UV-visible-NIR transmittance (T) spectra revealed a significant increase in transmittance values, specifically between 400 nm and 850 nm, as the concentration of by-pass in the composite progressively increases. This observation strongly supports the notion that including a by-pass markedly enhances the transmittance of the composite. This enhancement is attributed to the incident photon beam possessing sufficient energy to facilitate electron transfer from the valence band to the conduction band, with the remainder of the photon energy being absorbed by the samples. Notably, this effect is most pronounced in the by-pass15 sample, which boasts the highest by-pass concentration and consistently exhibits superior transmittance compared to the other samples. However, as we shift to higher wavelengths, the peak positions remain remarkably consistent across all concentrations, signifying the unaltered nature of electronic transitions.

Nevertheless, there is a slight variation in the intensity of these peaks associated with changing concentration. As we approach the wavelength range of 2100 nm to 2500 nm, the incident photon beam carries lower energy, reducing interactions with atomic structures within the composite. This suggests that by-pass plays a crucial role in enhancing the light–material interaction in the composite. Consequently, the composite with the highest by-pass concentration exhibits the strongest interactions with UV-visible-NIR light among all the samples examined, aligning well with the results reported in a previous study.[22]

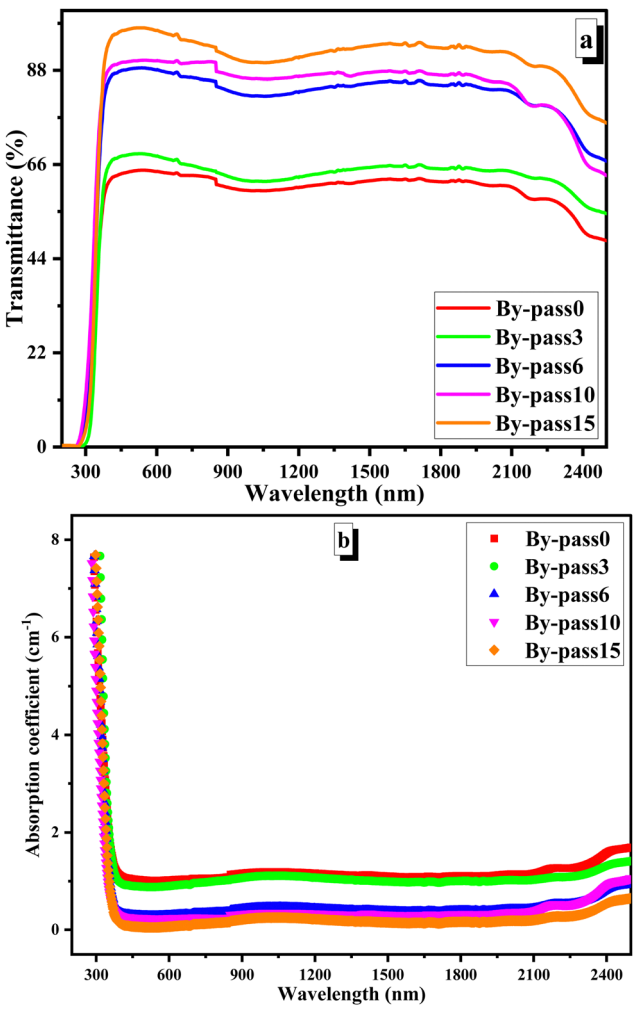

Fig. 3 (a) UV-visible-NIR transmittance profiles and (b) the absorption coefficient of the prepared samples.

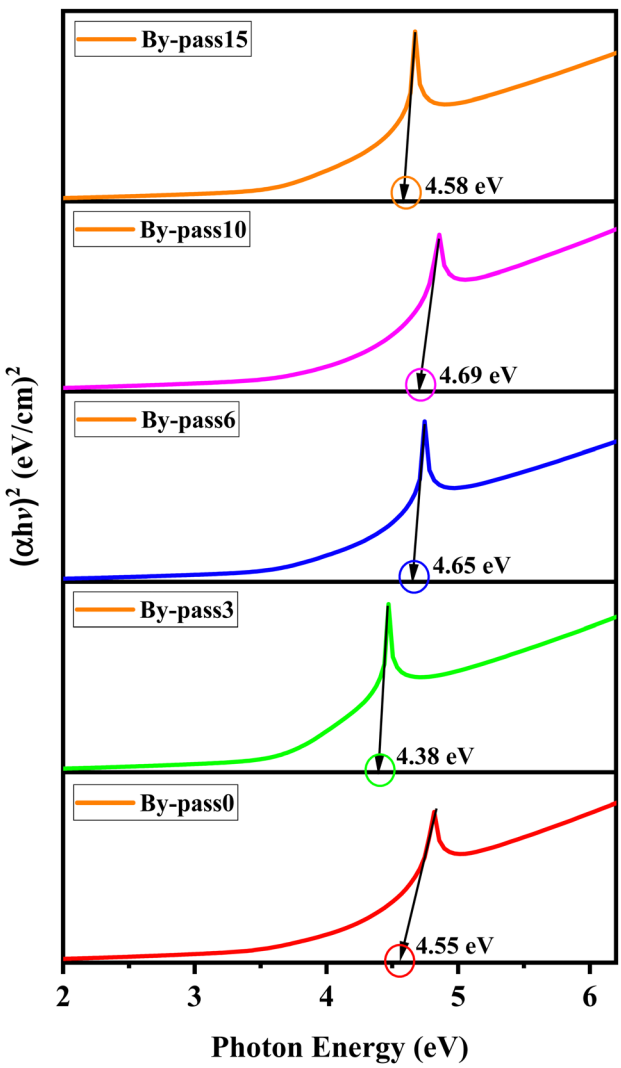

Fig. 4 Estimated direct band gap for different by-pass concentrations.

3.2.2. Bandgap energy. Determining the band gap of a material from its UV-visible-NIR transmission data involves plotting the transformed data to reveal the band gap as an intercept on the *x*-axis.

The Tauc plot is commonly used for this purpose. First, we need to approximate the absorption coefficient (α) from the transmittance (T) data using eqn (1):[35]

$$\alpha = -\left(\frac{\ln T}{t}\right) \quad (1)$$

where t is the thickness of the glass sample (cm), which in our work is t = 0.43 cm. As shown in Fig. 3(b), the absorption

Table 1 The direct band gaps for the composite at different concentrations of by-pass (*x*)

x (wt%)	Direct band gap (eV)
0	4.55
3	4.38
6	4.65
10	4.69
15	4.58

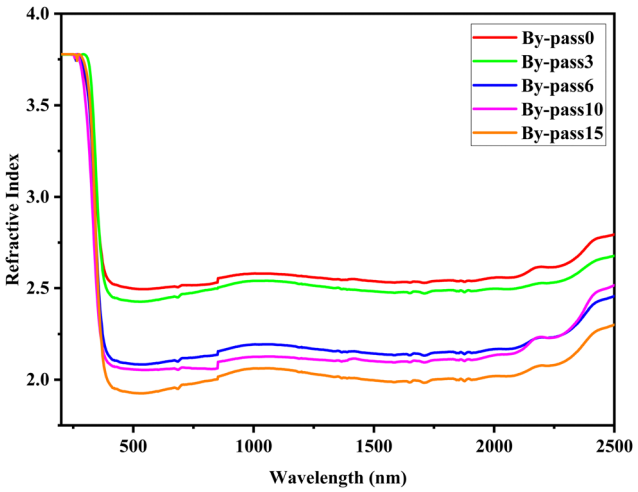

Fig. 5 The refractive index against the wavelength for different concentrations of by-pass in the studied samples.

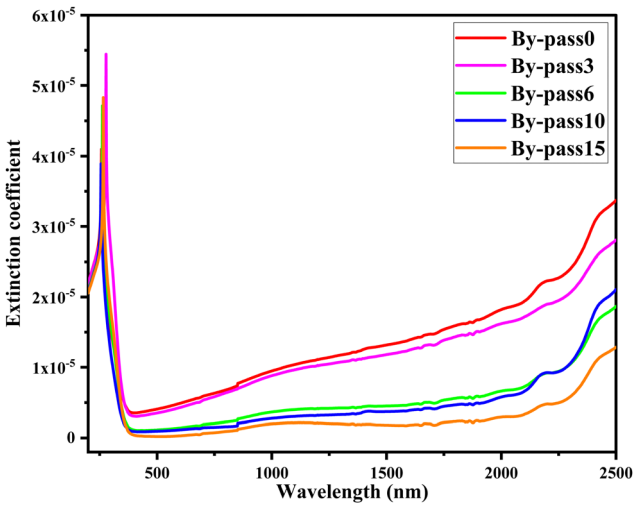

Fig. 6 The extinction coefficient against wavelength for different concentrations of by-pass in the studied samples.

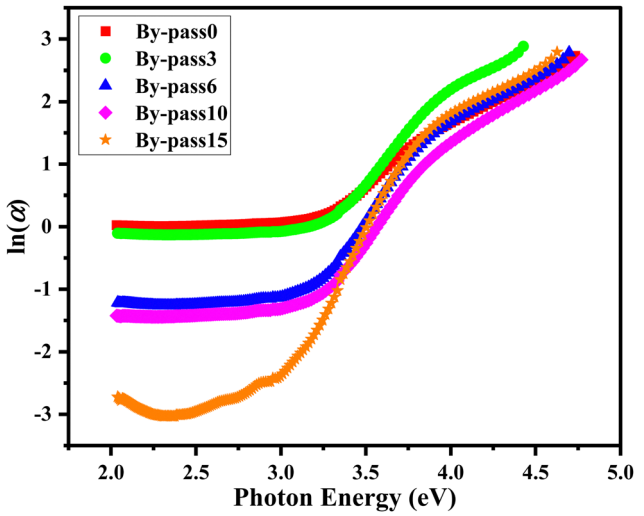

Fig. 7 The relationship between ln(α) and photon energy for different concentrations of by-pass in the studied samples.

Table 2 The Urbach energies (E_U) for the composite with different concentrations of by-pass (*x*)

x (wt%)	E_U (eV)
0	~0.421
3	~0.302
6	~0.244
10	~0.262
15	~0.183

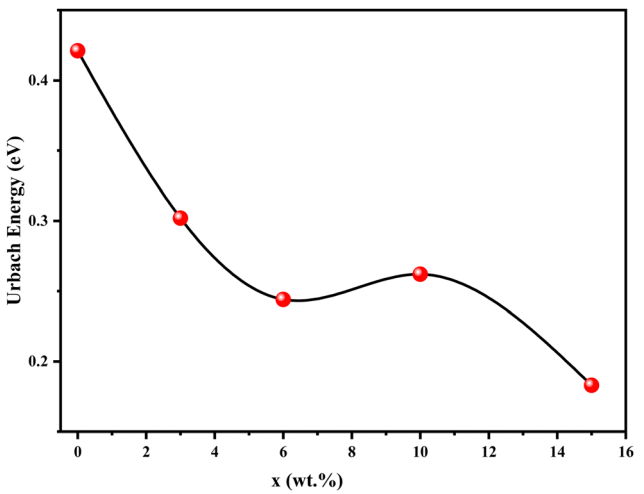

Fig. 8 The Urbach energy for different concentrations of by-pass (*x*) in the studied samples.

coefficient decreases sharply in the UV region but stabilizes in the visible-NIR areas, making this material ideal for opto-electronic applications.

The Tauc relationship is given by eqn (2):[36–38]

$$\alpha h\nu = A(h\nu - E_g)^n \quad (2)$$

where $h\nu$ is the photon energy (which can be calculated as $(1240/\lambda)$), where 1240 is a constant in eV and λ is the wavelength in nm, E_g is the optical band gap, A is a constant, and $n = 2$ for indirect transitions and $n = 1/2$ for direct transitions.

To determine the direct transition band gap, we can plot $((\alpha h\nu)^2)$ *vs.* $(h\nu)$. The direct optical band gap values are

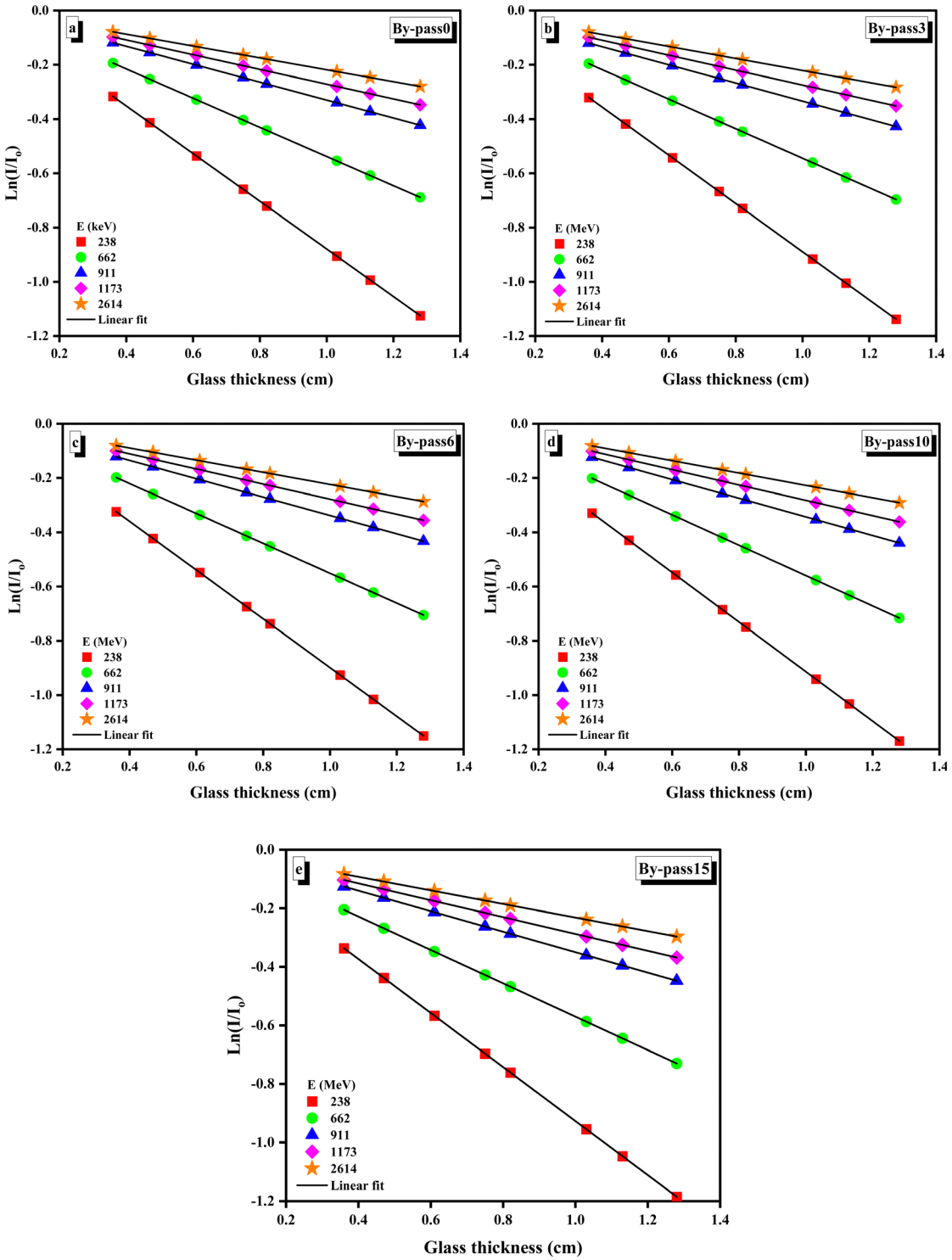

Fig. 9 (a)–(e) Transmission factor (ln(*I*/*I*$_0$)) against glass thickness at a selected photon energy.

determined by identifying the intercepts where the linear portion of the curve extrapolates to meet the linear axis representing photon energy. Fig. 4 shows that as the by-pass concentration increases from 0 to 15 wt%, the optical band gap energy changes, and the values are tabulated in Table 1. This increase implies that adding by-pass atoms to glass fabricates new energy levels in the band gap. These new energy levels act as traps for valence electrons, making the transition to high energy states in the conduction band more difficult.[39]

3.2.3. Refractive index. The refractive index (n) is a fundamental property of materials, indicating how much light is refracted as it passes through the material, which can be determined from the transmittance (T) data. The relationship of the refractive index is given by eqn (3):[40]

$$n = \left(\frac{1}{T-1}\right)^{\frac{1}{2}} + \frac{1}{T} \quad (3)$$

Fig. 5 illustrates the variation of the refractive index (n) as a function of wavelength. As the wavelength increases, "n" exhibits a general decreasing trend, which can be attributed to increased transmittance and reduced absorption due to traps and intraband transitions across varying concentrations of by-pass.

3.2.4. Extinction coefficient. The extinction coefficient, often represented by k, measures the amount of absorption loss when light passes through a material. It is closely related to the absorption coefficient (α) and provides insights into how efficiently a material can absorb light at a specific wavelength or photon energy. The relationship between "α" and "k" is given by eqn (4):[41]

$$k = \frac{\alpha\lambda}{4\pi} \quad (4)$$

where α is the absorption coefficient, which has been previously determined, and λ is the wavelength of light. Using eqn (4), the "k" value can be computed for each wavelength and different concentrations of by-pass in the composite. Fig. 6 shows "k" as a function of wavelength and by-pass concentration. The "k" value increases with wavelength, indicating that the glass absorbs and scatters more light at longer wavelengths. These results are well-matched with those obtained in previous studies.[22,42]

3.2.5. Urbach energy. Urbach energy (E_U) measures the width of the band tail states in disordered materials, which arise due to disorder and local potential fluctuations, leading to a non-zero density of states in the energy gap of a semiconductor. This parameter provides insights into the degree of disorder in the material. The "α" near the band edge of disordered materials can be described by the Urbach rule (eqn (5)):[43]

$$\alpha(E) = \alpha_0 \exp\left(\frac{E}{E_U}\right) \quad (5)$$

where $\alpha(E)$ is the absorption coefficient at photon energy (E), α_0 is a constant, and E_U can be determined by plotting ln(α) *versus* E and extracting the reciprocal of the slope, as shown in Fig. 7. A steeper slope indicates greater disorder in the material. The E_U values for the different concentrations of by-pass in the composite, extracted from the slope of the linear fit to ln(α) *vs.* photon energy, are tabulated in Table 2.

As shown in Fig. 8 and Table 2, the E_U has a notable trend observed where the E_U decreases from 0.421 eV at 0 wt% to 0.183 eV at 15 wt%. This indicates a significant reduction in disorder as the concentration of the by-pass component increases up to 15 wt%. The initial high value of E_U at 0 wt% suggests a high level of disorder in the pure composite material, likely due to inherent structural imperfections. The slight increase at 10 wt% may indicate a point of optimal concentration where additional by-pass does not further reduce disorder but instead introduces new forms of structural irregularities. As the by-pass concentration increases, these imperfections are gradually mitigated, leading to a more ordered structure and thus a lower E_U.[44,45]

The reduction in E_U with increasing by-pass concentration suggests an improvement in the structural order of the

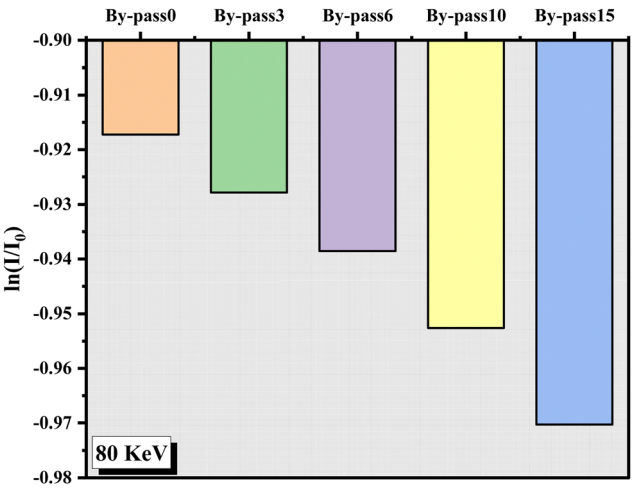

Fig. 10 ln(I/I_0) values against glass concentration at 80 keV.

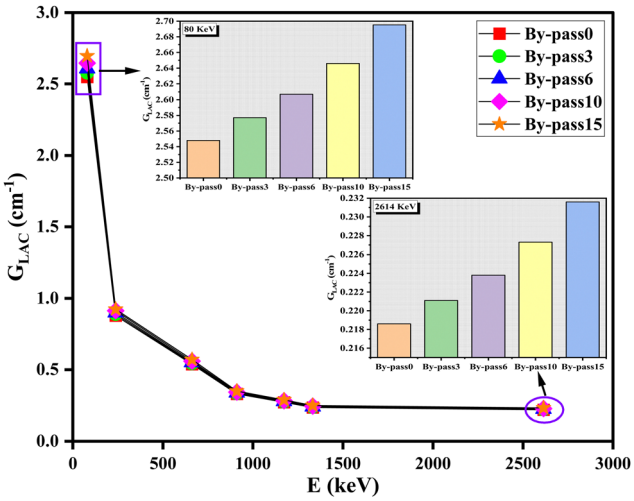

Fig. 11 Linear attenuation coefficient (G_{LAC}) against photon energy for all studied samples at a selected photon energy.

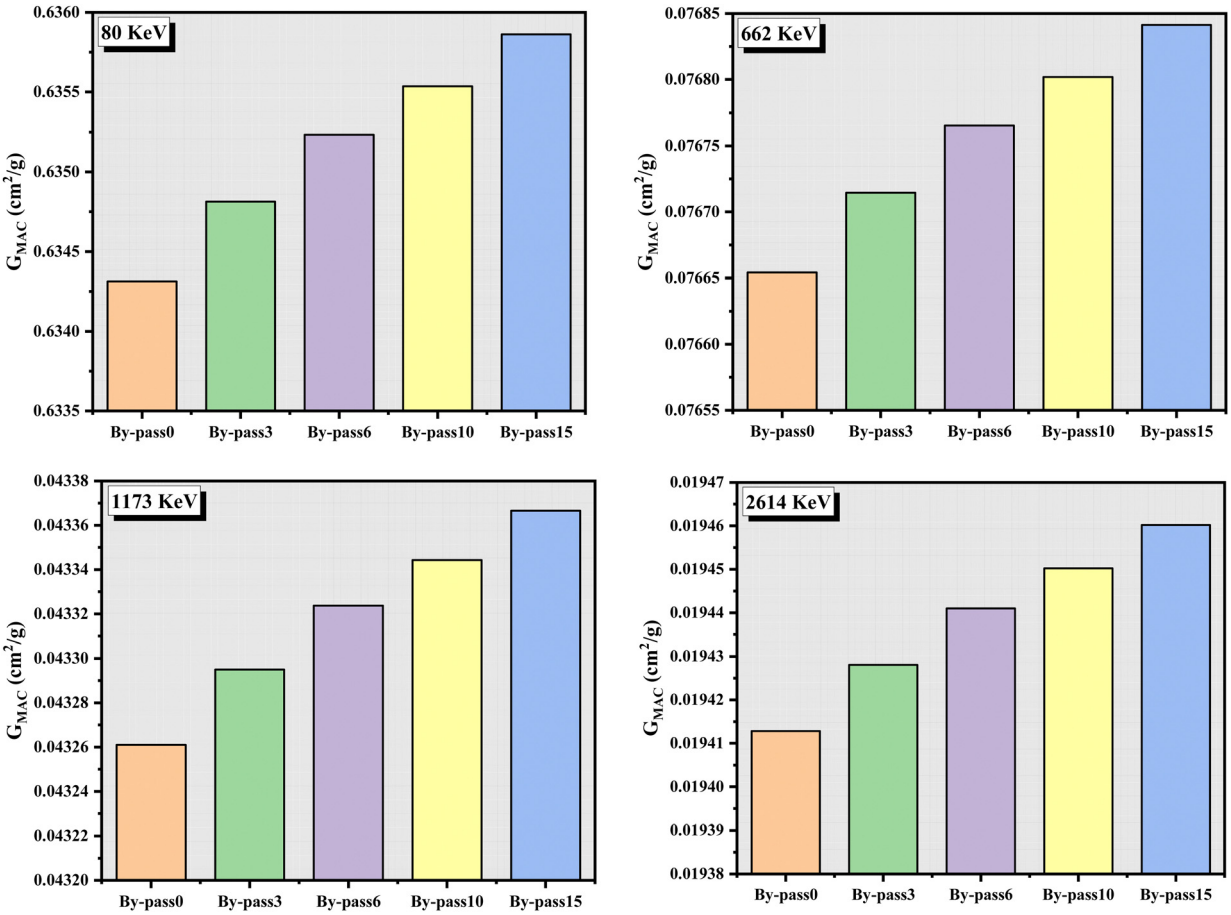

Fig. 12 Mass attenuation coefficient (G_{MAC}) against photon energy for all studied glasses at a selected photon energy.

Table 3 Mass attenuation coefficient for all glasses at selected photon energies

Sample	80 keV	238 keV	662 keV	911 keV	1173 keV	1333 keV	2614 keV
By-pass0	0.6343	0.2132	0.0767	0.0557	0.0433	0.0381	0.0194
By-pass3	0.6348	0.2134	0.0767	0.0557	0.0433	0.0381	0.0194
By-pass6	0.6352	0.2135	0.0768	0.0558	0.0433	0.0381	0.0194
By-pass10	0.6355	0.2136	0.0768	0.0558	0.0433	0.0381	0.0195
By-pass15	0.6359	0.2137	0.0768	0.0558	0.0434	0.0382	0.0195

composite material. This can have significant implications for applications that require high optical clarity and minimal electronic defects, such as photovoltaic devices, optical sensors, and transparent conductors. Future work should aim to understand the precise mechanisms by which the by-pass component mitigates disorder and explore the potential to optimize the concentration further to achieve the lowest possible E_U.

3.3. Radiation shielding properties

Fig. 9(a)–(e) shows a plot of $\ln(I/I_0)$ as a function of glass thickness for all the glasses studied at various energies. According to what is shown in this figure, the $\ln(I/I_0)$ values for by-pass0, by-pass3, by-pass6, by-pass10, and by-pass15 increase when the photon energy increases. In addition, at the studied energies, $\ln(I/I_0)$ values decrease with increasing by-pass.

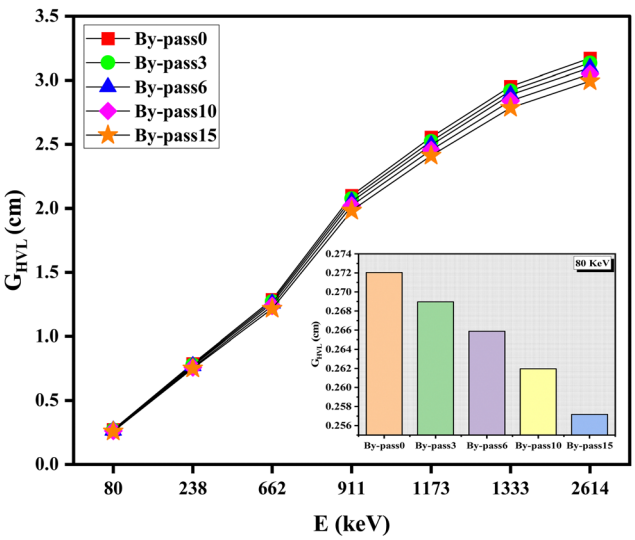

Fig. 13 Half value layer (G_{HVL}) against photon energy for all studied samples.

For example, at 662 keV $[\ln(I/I_0)]_{\text{by-pass0}} > [\ln(I/I_0)]_{\text{by-pass3}} > [\ln(I/I_0)]_{\text{by-pass6}} > [\ln(I/I_0)]_{\text{by-pass10}} > [\ln(I/I_0)]_{\text{by-pass15}}$. At a certain energy, for example, 80 keV, the $\ln(I/I_0)$ values for all glasses decrease as a function of glass compression. The $\ln(I/I_0)$ values are −0.92, −0.93, −0.94, −0.95, and −0.97 for by-pass0, by-pass3, by-pass6, by-pass10 and by-pass15 glasses, respectively (Fig. 10). This is because of the shift in density (D) that occurs while going from by-pass0 to by-pass3 to by-pass6 to by-pass10 to by-pass15. Moreover, the crystalline phases generated in by-pass15 are denser than those created in by-pass0, making the network structure more compact. The behavior of $\ln(I/I_0)$ with energy and glass composition also indicates that the photon attenuation lowers with increasing photon energy and increases with altering the amount of by-pass content. The slope between $\ln(I/I_0)$ and glass thickness has been used to measure the G_{LAC} values for by-pass0, by-pass3, by-pass6, by-pass10, and by-pass15 glass samples at different energies.

The G_{LAC} values for each studied glass are shown in Fig. 11 at the chosen photon energy. As can be seen from this figure, the G_{LAC} values for all glass ceramics decrease as the photon energy increases. This might be because there are three different ways in which photons can impart energy to matter. Glasses interact with gamma rays through the photoelectric effect, Compton scattering, and pair creation at low, medium, and high photon energies.[46–49] When measured at a specific energy (inset figures for 80 and 2614 keV, Fig. 11), the G_{LAC} values increase as the percentage of by-pass increases. The glass with the smallest G_{LAC} value is by-pass0, while the glass with the largest is by-pass15, which is well-matched with those obtained in a previous study.[50] The mass attenuation coefficient (G_{MAC}) results for all glasses, measured using glass density and G_{LAC} values, have been plotted at 80, 662, 1173, and 2614 keV in Fig. 12. All results are listed in Table 3. This table indicates that the G_{MAC} behaviors with photon energy and sample concentration are identical to G_{LAC} behaviors for all glasses.[51–54]

The half-value layers, denoted by G_{HVL}, and the mean free path, denoted by G_{MFP}, have been computed using the G_{LAC} values.[55] The values of G_{HVL} and G_{MFP} for all the tested glass samples are displayed in Fig. 13 and 14 at the chosen photon energy. As can be observed from these figures, the G_{HVL} and G_{MFP} values go up as the photon energy increases, but they go down when by-pass effects are considered. Compared to other glass samples, the by-pass15 sample, shown to have the maximum density among the glass ceramics researched, has the lowest G_{HVL} values at the tested photon energy, which is well-matched with those obtained in a previous study.[50]

Table 4 shows that the by-pass15 sample has the smallest G_{HVL} values, at 662, 1173, and 1333 keV than S1,[56] S2,[57] S3,[58] PCNKBi7.5,[59] Pb20,[60] PbG,[61] and S5[62] and different concrete samples (ordinary concrete (OC), hematite-serpentine (HSC), ilmenite-limonite (ILC), basalt-magnetite (BMC), and steel-scrap (SSC)).[63] This indicates that by-pass15 glass provides superior radiation protection, making it a highly efficient material for shielding applications. Fig. 15 and 16 present a comprehensive analysis of the radiation protection efficiency (RPE) for glasses with varying by-pass contents. Fig. 15 illustrates

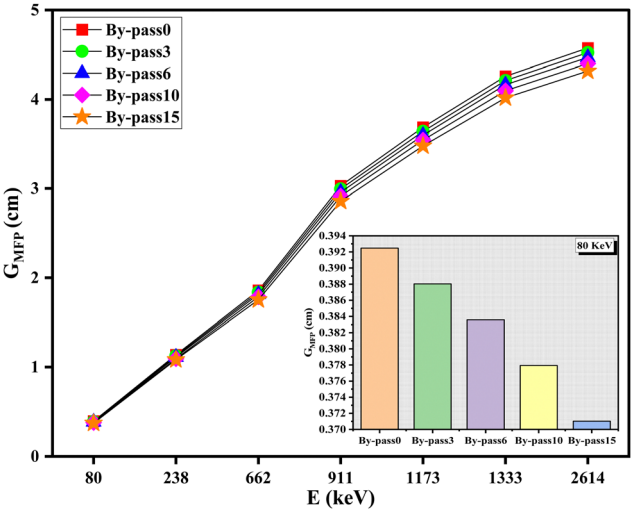

Fig. 14 Mean free path (G_{MFP}) against photon energy for all studied samples.

Table 4 Half value layer values of the by-pass15 glass sample compared to other glasses and concrete

	Half value layer (G_{HVL}) (cm)			
Sample	662 keV	1173 keV	1333 keV	Ref.
By-pass15	1.22	2.41	2.78	This work
S1	4.48	5.87	6.27	56
S2	3.80	4.99	5.32	57
S3	3.06	4.04	4.31	58
PCNKBi7.5	3.92	5.14	5.49	59
Pb20	3.85	5.13	5.48	60
PbG	3.77	4.95	5.28	61
S5	3.36	4.51	4.82	62
OC	3.80	4.98	5.31	63
HSC	3.62	4.75	5.07	
ILC	3.19	4.19	4.47	
BMC	2.98	3.91	4.17	
SSC	2.32	3.05	3.25	

the RPE as a function of glass thickness across a spectrum of photon energies for each by-pass concentration. It is immediately apparent that the RPE increases with increasing glass thickness, which is consistent with the expected behavior of gamma radiation attenuation. Notably, this increase in RPE is more pronounced in glasses with higher by-pass content, indicating that by-pass plays a significant role in enhancing the shielding properties of the glass. Fig. 16 compares the RPE at 80 and 2614 keV at two specific photon energies for the different by-pass concentrations. At a lower energy of 80 keV, the RPE is substantially higher across all samples, which indicates the more effective interaction of low-energy photons with the glass matrix. The by-pass15 sample exhibits the highest RPE at this energy, reinforcing that the by-pass content correlates with improved attenuation.

Conversely, at a higher energy of 2614 keV, there is an overall reduction in RPE for all samples, which aligns with the decreased efficiency of gamma-ray attenuation at higher energies due to the predominance of less interactive processes such as pair production. However, even at this higher energy, the

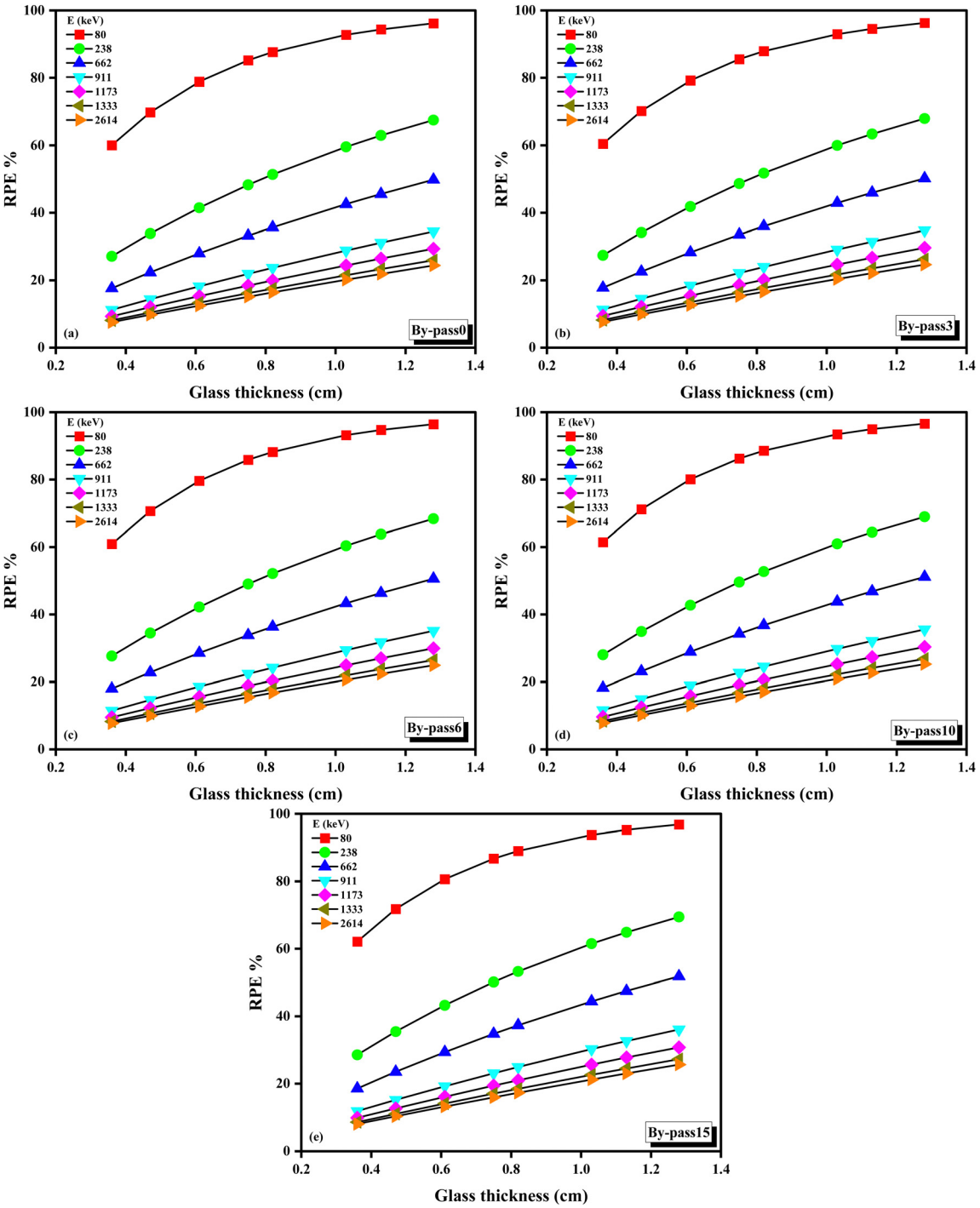

Fig. 15 (a)–(e) Radiation protection efficiency (RPE) for all studied samples at a selected photon energy.

by-pass15 sample maintains a higher RPE than the by-pass0 sample, though the difference is less marked than at 80 keV. This trend confirms the beneficial addition of by-pass to the glass, which not only contributes to increased density but may also introduce structural variations that favor photon attenuation. The interplay between by-pass concentration and RPE is complex and reflects the intricate balance of multiple factors. The compositional variation affects the density and atomic number, critical parameters for gamma-ray shielding.[64–67] By-pass components such as silica (SiO_2) and alumina (Al_2O_3) provide additional electron density, which is beneficial for the photoelectric effect at lower energies, while the increase in the overall atomic number enhances the probability of Compton scattering. As the photon energy escalates, these effects become less pronounced, yet the compositional benefits of by-pass are still evident. The data in Fig. 15 and 16 showcase the

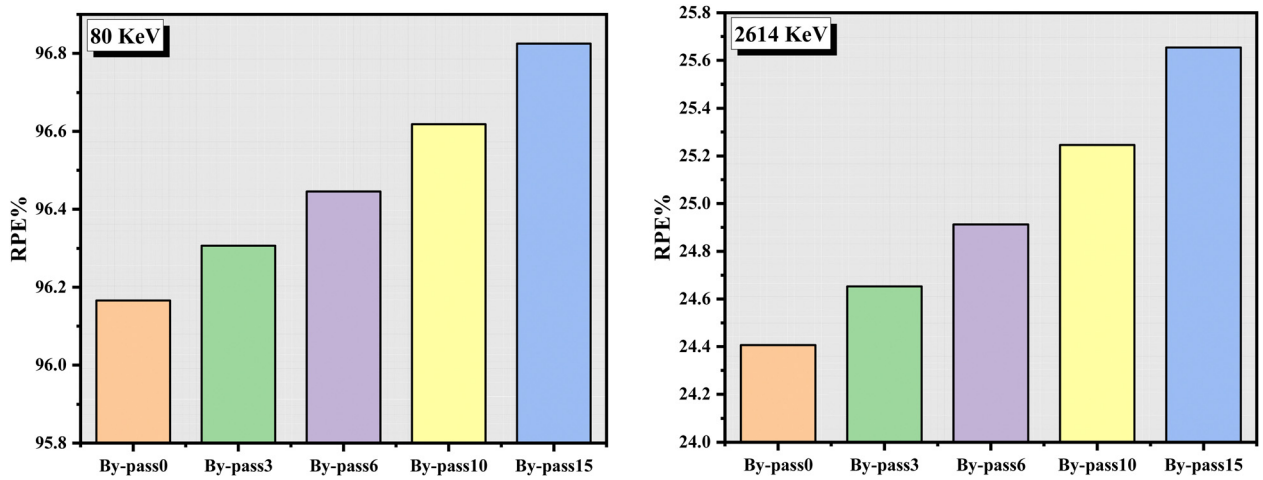

Fig. 16 Radiation protection efficiency (RPE) for all studied glasses at 80 and 2614 keV.

significance of glass composition, particularly the by-pass content, in dictating the RPE. The consistent pattern reinforces our hypothesis that by-pass waste, when integrated into glass matrices, can significantly improve the ability of the material to shield against gamma radiation, offering a dual benefit of waste utilization and enhanced protection against ionizing radiation.

4. Conclusions

The results present insightful data that could revolutionize the application of such glasses in gamma shielding endeavors. The XRD patterns of the glass samples confirmed their amorphous nature, denoting a broad scope of potential applications. In the optical domain, UV-visible analysis indicated an absorption surge between 400 and 850 nm as the by-pass concentration increased. Specifically, the by-pass15 sample displayed superior absorption, suggesting the pronounced role of by-pass in enhancing the absorption capacity of the composite. From the radiation shielding analysis, the by-pass15 sample outperformed its counterparts. The by-pass15 glass composition notably achieved the lowest half-value layer (G_{HVL}) measurements across the photon energies tested, with values at 662 keV, 1173 keV, and 1333 keV being lower than those of conventional materials like lead-based glass (Pb20 and PbG), indicating a superior radiation shielding capability. Furthermore, the radiation protection efficiency (RPE) of the by-pass15 glass showed a significant increase, outperforming the baseline by-pass0 composition by displaying RPE values that were consistently higher across all thicknesses, with the greatest differential observed at a lower photon energy of 80 keV. In light of these findings, the glasses, especially by-pass15, emerge as potential game-changers in the domain of radiation shielding. Their amorphous nature, enhanced absorption capabilities, and superior shielding properties position them as strong contenders in gamma radiation protection. The practical implications of our findings highlight the dual advantages of utilizing by-pass waste in glass composites: addressing environmental concerns and creating high-performance materials for optics and radiation protection. The versatility and effectiveness of these composites make them suitable for a wide range of applications, from medical and industrial uses to advanced technological and architectural implementations. Future research can further optimize these materials, potentially paving the way for safer and more efficient environments in industries relying heavily on radioactive isotopes.

Data availability

The data supporting the findings of this study, including all data presented in figures and tables, are available from the corresponding author, Dr Moustafa A. Darwish, upon reasonable request.

Conflicts of interest

The authors declare no competing interests.

References

1 G. Tyagi, A. Singhal, S. Routroy, D. Bhunia and M. Lahoti, A review on sustainable utilization of industrial wastes in radiation shielding concrete, *Mater. Today: Proc.*, 2020, **32**, 746–751, DOI: **10.1016/J.MATPR.2020.03.474**.
2 A. Kumar Sharma, N. Mishra and L. Chaudhary, Effect of adding marble-dust particles (MDP) as a partial cement replacement in concrete mix, *Mater. Today: Proc.*, 2023, DOI: **10.1016/j.matpr.2023.05.017**.
3 M. Dobiszewska, O. Bagcal, A. Beycioğlu, D. Goulias, F. Köksal, B. Płomiński and H. Ürünveren, Utilization of rock dust as cement replacement in cement composites: An alternative approach to sustainable mortar and concrete productions, *J. Build. Eng.*, 2023, **69**, 106180, DOI: **10.1016/J.JOBE.2023.106180**.

4 S. A. M. Issa, A. W. Alrowaily, C. Oche, A. M. A. Henaish, M. M. A. Halaka, N. S. Alatawi and H. M. H. Zakaly, Unveiling the potentials of polyvinyl alcohol/manganese chloride nanocomposites films: A detailed examination of their structural, spectral, and radiation properties, *Mater. Today Commun.*, 2023, **37**, 107177, DOI: **10.1016/J.MTCOMM.2023.107177**.

5 A. S. Ali, S. A. M. Issa, H. M. H. Zakaly, M. Rashad, I. Khan, B. Zhang, K. Akiyama, S. Kubuki and H. O. Tekin, Municipal waste slag for dyes photocatalytic and metal recovery applications through structural analysis and experimental characterization, *Int. J. Energy Res.*, 2021, **45**, 17691–17708, DOI: **10.1002/er.6884**.

6 A. El-Denglawey, H. M. H. Zakaly, K. Alshammari, S. A. M. Issa, H. O. Tekin, W. S. AbuShanab and Y. B. Saddeek, Prediction of mechanical and radiation parameters of glasses with high Bi_2O_3 concentration, *Results Phys.*, 2021, **21**, 103839, DOI: **10.1016/j.rinp.2021.103839**.

7 P. W. Ladenson, L. E. Braverman, E. L. Mazzaferri, F. Brucker-Davis, D. S. Cooper, J. R. Garber, F. E. Wondisford, T. F. Davies, L. J. DeGroot, G. H. Daniels, D. S. Ross, B. D. Weintraub, I. D. Hay, S. Levis, J. C. Reynolds, J. Robbins, D. V. Becker, R. R. Cavalieri, H. R. Maxon, K. McEllin and R. Moscicki, Comparison of Administration of Recombinant Human Thyrotropin with Withdrawal of Thyroid Hormone for Radioactive Iodine Scanning in Patients with Thyroid Carcinoma, *N. Engl. J. Med.*, 1997, **337**, 888–896, DOI: **10.1056/NEJM199709253371304**.

8 H. O. Tekin, G. ALMisned, Y. S. Rammah, E. M. Ahmed, F. T. Ali, D. Sen Baykal, W. Elshami, H. M. H. Zakaly, S. A. M. Issa, G. Kilic and A. Ene, Transmission factors, mechanical, and gamma ray attenuation properties of barium-phosphate-tungsten glasses: Incorporation impact of WO_3, *Optik*, 2022, **267**, 169643, DOI: **10.1016/j.ijleo.2022.169643**.

9 I. R. Miousse, K. R. Kutanzi and I. Koturbash, Effects of ionizing radiation on DNA methylation: from experimental biology to clinical applications, *Int. J. Radiat. Biol.*, 2017, **93**, 457–469, DOI: **10.1080/09553002.2017.1287454**.

10 Y. Al-Hadeethi, M. S. Al-Buriahi and M. I. Sayyed, Bioactive glasses and the impact of Si_3N_4 doping on the photon attenuation up to radiotherapy energies, *Ceram. Int.*, 2020, **46**, 5306–5314, DOI: **10.1016/j.ceramint.2019.10.281**.

11 S. A. M. Issa, H. M. H. Zakaly, M. Rashad, A. S. Ali and H. O. Tekin, Fabrication, optical, structural, and gamma-ray attenuation properties of novel slag-waste glasses as superior shields: An exploring journey for waste to glass transformation, *Optik*, 2022, **270**, 169999, DOI: **10.1016/j.ijleo.2022.169999**.

12 G. ALMisned, W. Elshami, S. Issa, G. Susoy, H. Zakaly, M. Algethami, Y. Rammah, A. Ene, S. Al-Ghamdi, A. Ibraheem and H. Tekin, Enhancement of Gamma-ray Shielding Properties in Cobalt-Doped Heavy Metal Borate Glasses: The Role of Lanthanum Oxide Reinforcement, *Materials*, 2021, **14**, 7703, DOI: **10.3390/ma14247703**.

13 U. Perişanoğlu, F. I. El-Agawany, E. Kavaz, M. Al-Buriahi and Y. S. Rammah, Surveying of Na_2O_3–BaO–PbO–Nb_2O_5–SiO_2–Al_2O_3 glass-ceramics system in terms of alpha, proton, neutron and gamma protection features by utilizing GEANT4 simulation codes, *Ceram. Int.*, 2020, **46**, 3190–3202, DOI: **10.1016/J.CERAMINT.2019.10.023**.

14 G. Susoy, E. E. A. Guclu, O. Kilicoglu, M. Kamislioglu, M. S. Al-Buriahi, M. M. Abuzaid and H. O. Tekin, The impact of Cr_2O_3 additive on nuclear radiation shielding properties of LiF–SrO–B_2O_3 glass system, *Mater. Chem. Phys.*, 2020, **242**, 122481, DOI: **10.1016/J.MATCHEMPHYS.2019.122481**.

15 H. M. H. Zakaly, I. M. Nabil, S. A. M. Issa, N. Almousa, Z. Y. Khattari and Y. S. Rammah, Probing the elasticity and radiation protection potential of neodymium(III) doped zinc and niobium tellurite glasses: An integrated simulated and applied physics perspective, *Mater. Today Commun.*, 2023, **37**, 107113, DOI: **10.1016/j.mtcomm.2023.107113**.

16 A. M. A. Mostafa, S. A. M. Issa and M. I. Sayyed, Gamma ray shielding properties of PbO-B_2O_3-P_2O_5 doped with WO_3, *J. Alloys Compd.*, 2017, **708**, 294–300, DOI: **10.1016/j.jallcom.2017.02.303**.

17 S. A. M. Issa, M. I. Sayyed, A. M. A. Mostafa, G. Lakshminarayana and I. V. Kityk, Investigation of mechanical and radiation shielding features of heavy metal oxide based phosphate glasses for gamma radiation attenuation applications, *J. Mater. Sci.: Mater. Electron.*, 2019, **30**, 12140–12151, DOI: **10.1007/S10854-019-01572-X/FIGURES/15**.

18 H. M. H. Zakaly, S. A. M. Issa, H. O. Tekin, A. Badawi, H. A. Saudi, A. M. A. Henaish and Y. S. Rammah, An experimental evaluation of CdO/PbO–B_2O_3 glasses containing neodymium oxide: Structure, electrical conductivity, and gamma-ray resistance, *Mater. Res. Bull.*, 2022, 111828, DOI: **10.1016/j.materresbull.2022.111828**.

19 B. Aktas, M. Albaskar, S. Yalcin and K. Dogru, Optical properties of soda-lime-silica glasses doped with peanut shell powder, *Arch. Mater. Sci. Eng.*, 2016, **82**, 57–61, DOI: **10.5604/01.3001.0009.7104**.

20 B. Çetin, Yalçin, B. Aktaş and M. Albaşkara, Investigation of radiation shielding properties of soda-lime-silica glasses doped with different food materials, *Acta Phys. Pol., A*, 2017, **132**, 988–990, DOI: **10.12693/APhysPolA.132.988**.

21 B. Aktas, M. Albaskara, S. Yalcin and K. Dogru, Optical properties of soda-lime-silica glasses doped with eggshell powder, *Acta Phys. Pol., A*, 2017, **132**, 442–444, DOI: **10.12693/APHYSPOLA.132.442**.

22 A. I. Elazaka, H. M. H. Zakaly, S. A. M. Issa, M. Rashad, H. O. Tekin, H. A. Saudi, V. H. Gillette, T. T. Erguzel and A. G. Mostafa, New approach to removal of hazardous Bypass Cement Dust (BCD) from the environment: $20Na_2O$–$20BaCl_2$–$(60 - x)B_2O_3$-(x)BCD glass system and Optical, mechanical, structural and nuclear radiation shielding competences, *J. Hazard. Mater.*, 2021, **403**, 123738, DOI: **10.1016/j.jhazmat.2020.123738**.

23 M. I. Sayyed, Radiation shielding characterization of a Yb:CaBTeX glass system as a function of TeO_2 concentration, *Opt. Quantum Electron.*, 2024, **56**, 1–11, DOI: **10.1007/s11082-023-05951-x**.

24 M. Y. Hanfi, M. I. Sayyed, E. Lacomme, I. Akkurt and K. A. Mahmoud, The influence of MgO on the radiation protection

and mechanical properties of tellurite glasses, *Nucl. Eng. Technol.*, 2021, **53**, 2000–2010, DOI: 10.1016/j.net.2020.12.012.

25 M. Y. Hanfi, M. I. Sayyed, E. Lacomme, I. Akkurt and K. A. Mahmoud, The influence of MgO on the radiation protection and mechanical properties of tellurite glasses, *Nucl. Eng. Technol.*, 2021, **53**, 2000–2010, DOI: 10.1016/j.net.2020.12.012.

26 M. I. Sayyed, Effect of WO_3 on the attenuation parameters of TeO_2–La_2O_3–WO_3 glasses for radiation shielding application, *Radiat. Phys. Chem.*, 2024, **215**, 111319, DOI: 10.1016/j.radphyschem.2023.111319.

27 H. M. H. Zakaly, H. A. Saudi, H. O. Tekin, M. Rashad, S. A. M. Issa, Y. S. Rammah, A. I. Elazaka, M. M. Hessien and A. Ene, Glass fabrication using ceramic and porcelain recycled waste and lithium niobate: physical, structural, optical and nuclear radiation attenuation properties, *J. Mater. Res. Technol.*, 2021, **15**, 4074–4085, DOI: 10.1016/j.jmrt.2021.09.138.

28 Z. Ghouleh and Y. Shao, Turning municipal solid waste incineration into a cleaner cement production, *J. Cleaner Prod.*, 2018, **195**, 268–279, DOI: 10.1016/j.jclepro.2018.05.209.

29 G. ALMisned, D. Sen Baykal, G. Kilic, E. Ilik, E. Rabaa, G. Susoy, H. M. H. Zakaly, A. Ene and H. O. Tekin, Comparative analysis on application conditions of indium (III) oxide-reinforced glasses in nuclear waste management and source transportation: A Monte Carlo simulation study, *Heliyon*, 2023, **9**, e14274, DOI: 10.1016/j.heliyon.2023.e14274.

30 M. I. A. Abdel Maksoud, O. I. Sallam, S. M. Kassem, R. A. Fahim and A. S. Awed, Novel Strategy for Hazardous Cement Bypass Dust Removal: Structural, Optical and Nuclear Radiation Shielding Properties of CBD-Bismuth Borate Glass, *J. Inorg. Organomet. Polym. Mater.*, 2022, **32**, 3533–3545, DOI: 10.1007/s10904-022-02378-x.

31 Y. B. Saddeek, G. Y. Mohamed, H. Shokry Hassan, A. M. A. Mostafa and G. Abd Elfadeel, Effect of gamma irradiation on the FTIR of cement kiln dust-bismuth borate glasses, *J. Non-Cryst. Solids*, 2015, **419**, 110–117, DOI: 10.1016/j.jnoncrysol.2015.03.021.

32 C. Gautam, A. Madheshiya, A. Kumar Singh, K. Kishor Dey and M. Ghosh, Synthesis, optical and solid NMR studies of strontium titanate borosilicate glasses doped with TeO_2, *Results Phys.*, 2020, **16**, 102914, DOI: 10.1016/J.RINP.2019.102914.

33 A. Madheshiya, C. Gautam and S. Kumar, Synthesis, structural and X-ray absorption spectroscopy of $(Pb_xBi_{1-x})\cdot TiO_3$ borosilicate glass and glass ceramics, *J. Asian Ceram. Soc.*, 2017, **5**, 276–283, DOI: 10.1016/J.JASCER.2017.05.003.

34 J. Cho, G. R. Waetzig, M. Udayakantha, C. Y. Hong and S. Banerjee, Incorporation of Hydroxyethylcellulose-Functionalized Halloysite as a Means of Decreasing the Thermal Conductivity of Oilwell Cement, *Sci. Rep.*, 2018, **8**(1), 16149, DOI: 10.1038/s41598-018-34283-0.

35 S. Yasmeen, F. Iqbal, T. Munawar, M. A. Nawaz, M. Asghar and A. Hussain, Synthesis, structural and optical analysis of surfactant assisted ZnO–NiO nanocomposites prepared by homogeneous precipitation method, *Ceram. Int.*, 2019, **45**, 17859–17873, DOI: 10.1016/J.CERAMINT.2019.06.001.

36 S. Roy, M. P. Ghosh and S. Mukherjee, Introducing magnetic properties in Fe-doped ZnO nanoparticles, *Appl. Phys. A: Mater. Sci. Process.*, 2021, **127**, 451, DOI: 10.1007/s00339-021-04580-z.

37 M. K. Halimah, M. F. Faznny, M. N. Azlan and H. A. A. Sidek, Optical basicity and electronic polarizability of zinc borotellurite glass doped La^{3+} ions, *Results Phys.*, 2017, **7**, 581–589, DOI: 10.1016/J.RINP.2017.01.014.

38 A. Kumar, R. Kaur, M. I. Sayyed, M. Rashad, M. Singh and A. M. Ali, Physical, structural, optical and gamma ray shielding behavior of $(20 + x)$ PbO–10BaO–10Na_2O–10MgO–$(50 - x)$ B_2O_3 glasses, *Phys. B*, 2019, **552**, 110–118, DOI: 10.1016/J.PHYSB.2018.10.001.

39 M. Mazilu, N. Tigau and V. Musat, Optical properties of undoped and Al-doped ZnO nanostructures grown from aqueous solution on glass substrate, *Opt. Mater.*, 2012, **34**, 1833–1838, DOI: 10.1016/J.OPTMAT.2012.05.010.

40 M. A. Ditta, M. A. Farrukh, S. Ali and N. Younas, X-ray peak profiling, optical parameters and catalytic properties of pure and CdS doped ZnO–NiO nanocomposites, *Russ. J. Appl. Chem.*, 2017, **90**, 151–159, DOI: 10.1134/S1070427217010220/METRICS.

41 A. S. Hassanien and A. A. Akl, Influence of composition on optical and dispersion parameters of thermally evaporated non-crystalline $Cd_{50}S_{50-x}Se_x$ thin films, *J. Alloys Compd.*, 2015, **648**, 280–290, DOI: 10.1016/J.JALLCOM.2015.06.231.

42 F. K. Shan and Y. S. Yu, Band gap energy of pure and Al-doped ZnO thin films, *J. Eur. Ceram. Soc.*, 2004, **24**, 1869–1872, DOI: 10.1016/S0955-2219(03)00490-4.

43 F. Migliorini, S. Belmuso, R. Dondè, S. De Iuliis and I. Altman, To optical properties of carbon nanoparticles: A need in comprehending Urbach energy, *Carbon Trends*, 2022, **8**, 100184, DOI: 10.1016/j.cartre.2022.100184.

44 G. Upender, S. Ramesh, M. Prasad, V. G. Sathe and V. C. Mouli, Optical band gap, glass transition temperature and structural studies of $(100 - 2x)TeO_2$–xAg_2O–xWO_3 glass system, *J. Alloys Compd.*, 2010, **504**, 468–474, DOI: 10.1016/j.jallcom.2010.06.006.

45 U. G. Issever, G. Kilic and E. Ilik, The Impact of CuO on physical, structural, optical and thermal properties of dark VPB semiconducting glasses, *Opt. Mater.*, 2021, **116**, 111084, DOI: 10.1016/j.optmat.2021.111084.

46 H. M. H. Zakaly, D. E. Abulyazied, H. A. Saudi, B. M. Alotaibi and S. A. M. Issa, Surface hardness, thermal, optical, and photon attenuation coefficients assessment for dysprosium-doped tellurite glasses, *J. Rare Earths*, 2023, **41**, 1083–1090, DOI: 10.1016/J.JRE.2022.05.009.

47 M. I. Sayyed, S. A. M. Issa and S. H. Auda, Assessment of radioprotective properties of some anti-inflammatory drugs, *Prog. Nucl. Energy*, 2017, **100**, 297–308, DOI: 10.1016/j.pnucene.2017.07.003.

48 H. M. H. Zakaly, D. E. Abulyazied, S. A. M. Issa, A. W. Alrowaily, H. A. Saudi and H. M. Abomostafa, Optical, Microhardness, and Radiation Shielding Properties of Rare Earth Doped Strontium Barium Titanate Polyvinylidene Fluoride Nanocomposites, *J. Inorg. Organomet. Polym. Mater.*, 2023, **33**, 1177–1190, DOI: 10.1007/S10904-023-02564-5.

49 H. M. H. Zakaly, H. O. Tekin, A. M. S. Issa, A. W. Alrowaily, A. Ene and Y. S. Rammah, Dual Impacts of Bi2O3/B2O3 Substitution on Mechanical and Attenuation Properties of Zinc–Bismuth–Borate Ternary Glasses for Diagnosis γ-Rays Shielding Materials Application, *J. Inorg. Organomet. Polym. Mater.*, 2023, **33**, 1495–1506, DOI: **10.1007/s10904-022-02527-2**.

50 M. S. Eid, I. I. Bondouk, H. M. Saleh, K. M. Omar, M. I. Sayyed, A. M. El-Khatib and M. Elsafi, Implementation of waste silicate glass into composition of ordinary cement for radiation shielding applications, *Nucl. Eng. Technol.*, 2022, **54**, 1456–1463, DOI: **10.1016/j.net.2021.10.007**.

51 A. S. Abouhaswa, H. M. H. Zakaly, S. A. M. Issa, M. Rashad, M. Pyshkina, H. O. Tekin, R. El-Mallawany and M. Y. A. Mostafa, Synthesis, physical, optical, mechanical, and radiation attenuation properties of TiO_2–Na_2O–Bi_2O_3–B_2O_3 glasses, *Ceram. Int.*, 2021, **47**, 185–204, DOI: **10.1016/j.ceramint.2020.08.122**.

52 G. Kilic, S. A. M. Issa, E. Ilik, O. Kilicoglu and H. O. Tekin, A journey for exploration of Eu_2O_3 reinforcement effect on zinc-borate glasses: Synthesis, optical, physical and nuclear radiation shielding properties, *Ceram. Int.*, 2021, **47**, 2572–2583, DOI: **10.1016/j.ceramint.2020.09.103**.

53 A. M. A. Mostafa, H. M. Zakaly, S. A. Al-Ghamdi, S. A. Issa, M. Al-Zaibani, R. M. Ramadan and E. F. El Agammy, PbO–Sb_2O_3–B_2O_3–CuO glassy system: Evaluation of optical, gamma and neutron shielding properties, *Mater. Chem. Phys.*, 2021, **258**, 123937, DOI: **10.1016/j.matchemphys.2020.123937**.

54 H. O. Tekin, G. ALMisned, H. M. H. Zakaly, A. Zamil, D. Khoucheich, G. Bilal, L. Al-Sammarraie, S. A. M. Issa, M. S. Al-Buriahi and A. Ene, Gamma, neutron, and heavy charged ion shielding properties of Er^{3+}-doped and Sm^{3+}-doped zinc borate glasses, *Open Chem.*, 2022, **20**, 130–145, DOI: **10.1515/CHEM-2022-0128**.

55 N. Almousa, S. A. M. Issa, M. M. Salem, M. A. Darwish, E. N. Serag, S. N. Nazrin and H. M. H. Zakaly, Tailoring perovskite ceramics for improved structure, vibrational behaviors and radiation protection: The role of lanthanum in $PbTiO_3$, *Opt. Mater.*, 2024, **152**, 115543, DOI: **10.1016/j.optmat.2024.115543**.

56 B. Aktas, S. Yalcin, K. Dogru, Z. Uzunoglu and D. Yilmaz, Structural and radiation shielding properties of chromium oxide doped borosilicate glass, *Radiat. Phys. Chem.*, 2019, **156**, 144–149, DOI: **10.1016/J.RADPHYSCHEM.2018.11.012**.

57 S. Yalcin, B. Aktas and D. Yilmaz, Radiation shielding properties of Cerium oxide and Erbium oxide doped obsidian glass, *Radiat. Phys. Chem.*, 2019, **160**, 83–88, DOI: **10.1016/J.RADPHYSCHEM.2019.03.024**.

58 M. H. A. Mhareb, Y. S. M. Alajerami, M. I. Sayyed, N. Dwaikat, M. Alqahtani, F. Alshahri, N. Saleh, N. Alonizan, T. Ghrib and S. I. Al-Dhafar, Radiation shielding, structural, physical, and optical properties for a series of borosilicate glass, *J. Non-Cryst. Solids*, 2020, **550**, 120360, DOI: **10.1016/J.JNONCRYSOL.2020.120360**.

59 H. A. Al-Yousef, M. I. Sayyed, M. Alotiby, A. Kumar, Y. S. Alghamdi, B. M. Alotaibi, N. A. M. Alsaif, K. A. Mahmoud and Y. Al-Hadeethi, Evaluation of optical, and radiation shielding features of New phosphate-based glass system, *Optik*, 2021, **242**, 167220, DOI: **10.1016/J.IJLEO.2021.167220**.

60 A. H. Almuqrin, A. Kumar, J. F. M. Jecong, N. Al-Harbi, E. Hannachi and M. I. Sayyed, Li_2O–K_2O–B_2O_3–PbO glass system: Optical and gamma-ray shielding investigations, *Optik*, 2021, **247**, 167792, DOI: **10.1016/J.IJLEO.2021.167792**.

61 F. F. Al-Harbi, N. S. Prabhu, M. I. Sayyed, A. H. Almuqrin, A. Kumar and S. D. Kamath, Evaluation of structural and gamma ray shielding competence of Li_2O–K_2O–B_2O_3–HMO (HMO = SrO/TeO_2/PbO/Bi_2O_3) glass system, *Optik*, 2021, **248**, 168074, DOI: **10.1016/J.IJLEO.2021.168074**.

62 S. Singh, R. Kaur, S. Rani and B. S. Sidhu, Physical, structural and nuclear radiation shielding behaviour of xBaO–(0.30 − x)MgO–0.10Na_2O–0.10Al_2O_3–0.50B_2O_3 glass matrix, *Mater. Chem. Phys.*, 2022, **276**, 125415, DOI: **10.1016/J.MATCHEMPHYS.2021.125415**.

63 I. I. Bashter, Calculation of radiation attenuation coefficients for shielding concretes, *Ann. Nucl. Energy*, 1997, **24**, 1389–1401, DOI: **10.1016/S0306-4549(97)00003-0**.

64 I. S. Mahmoud, S. A. M. Issa, H. M. H. Zakaly, H. A. Saudi, A. S. Ali, Y. B. Saddeek, T. Alharbi and H. O. Tekin, Material characterization of WO_3/Bi_2O_3 substituted calcium–borosilicate glasses: Structural, physical, mechanical properties and gamma-ray resistance competencies, *J. Alloys Compd.*, 2021, **888**, 161419, DOI: **10.1016/j.jallcom.2021.161419**.

65 A. M. Madbouly, O. I. Sallam, S. A. M. Issa, M. Rashad, A. Hamdy, H. O. Tekin and H. M. H. Zakaly, Experimental and FLUKA evaluation on structure and optical properties and γ-radiation shielding capacity of bismuth borophosphate glasses, *Prog. Nucl. Energy*, 2022, **148**, 104219, DOI: **10.1016/J.PNUCENE.2022.104219**.

66 S. A. M. Issa, A. M. Almutairi, K. Albalawi, O. K. Dakhilallah, H. M. H. Zakaly, A. Ene, D. E. Abulyazied, S. M. Ahmed, R. A. Youness and M. A. Taha, Production of Hybrid Nanocomposites Based on Iron Waste Reinforced with Niobium Carbide/Granite Nanoparticles with Outstanding Strength and Wear Resistance for Use in Industrial Applications, *Nanomaterials*, 2023, **13**, 537, DOI: **10.3390/nano13030537**.

67 A. M. Abd-Elnaiem, H. A. Saudi, H. M. H. Zakaly, S. A. M. Issa and M. Rashad, The effect of composition and γ-irradiation on the Vickers hardness, structural and optical properties of $x$$LiNbO_3$–25CaO–35PbO–(40 − x) waste systems, *Ceram. Int.*, 2021, **47**, 18751–18760, DOI: **10.1016/j.ceramint.2021.03.210**.